Faculteit Bètawetenschappen

In-situ Transmission Electron Microscopy Investigation of WS_2 Growth Mechanisms and Density Functional Theory Calculations on WS_2

Jesse Bückmann

Natuur- en Sterrenkunde & Scheikunde

Supervisors:

Dr. Marijn van Huis SUPERVISOR
Soft Condensed Matter

MSc. Dnyaneshwar Gavhane SUPERVISOR
Soft Condensed Matter

June 11, 2020

Abstract
Growth processes of WS_2 have been studied via in-situ Transmission Electrons Microscopy (TEM) heating experiments. DFT calculations were performed on WS_2 to investigate how magnetic properties affect the band-gap. TEM heating experiments taught us, that lattices grow in the temperature range of 100-800 °C and faceting occurred at 450 °C. With EDX spectroscopy a ratio of 1:2 for W:S has been found, confirming that WS_2 is, indeed, formed. DFT calculations indicated that the WS_2 structure is not magnetic. However, when magnetic properties are enforced, the band-gap and the fermi-energy is altered. External electric fields can thus be used for band-gap tuning, making WS_2 a viable semi-conductor.

Keywords: Transmission Electron Microscopy, Density Functional Theory, tungsten disulfide, vertically grown sheets, hexagonal lattices, spin-orbit coupling, VASP, in-situ, 2D nanomaterials

Contents

1 Introduction **1**

2 Theory **1**
2.1 Transmission Electron Microscopy (TEM) . . . 1
2.1.1 Heating chip . . . 3
2.1.2 Drop casting and imaging . . . 3
2.2 Energy Dispersive X-ray Spectroscopy(EDX) . . . 4
2.3 Density Functional Theory (DFT) . . . 4
2.3.1 Theory . . . 4
2.3.2 VASP . . . 5
2.3.3 Method . . . 5
2.3.4 K-point spacing . . . 6
2.3.5 Van der Waals functionals . . . 6
2.3.6 Spin-orbit coupling (SOC) . . . 6

3 Results **7**
3.1 TEM results . . . 7
3.2 EDX results . . . 12
3.3 DFT Results . . . 12
3.3.1 Van der Waals functionals . . . 12
3.3.2 Magnetisation . . . 13
3.3.3 Spin-Orbit Coupling (SOC) and bandgaps . . . 13

4 Discussion **16**

5 Conclusion and outlook **17**

A Benchmarking Results **IV**

B Additional images **V**

C Spin-Orbit Coupling **VII**

D Band structures **VIII**

1 Introduction

Developments in science are the result of discoveries of new materials and new applications of these materials. Whenever a new material, with interesting and useful properties, is discovered, it will receive a lot of attention and is typically followed up by extensive research. Therefore, it came as no surprise that the discovery of graphene brought so much research to the field of 2D materials.[1]

Graphene was discovered in 2004 and was extracted from graphite by the so-called scotch tape method, which is a mechanical exfoliation method.[2] This method relies on the principle that the in-plane bonds are significantly stronger than the van der Waals interactions that binds different layers together.[3] What makes graphene so special is its high mechanical strength, the fact that it is very light and highly conducting. Thanks to its properties graphene has already found many applications in technology, energy storage, etc. . [4]

Since graphene was so widely applicable, the field of 2D materials became one of substantial research. [5, 6, 7] . Quantum confined nanomaterials, such as 2D materials, have as characteristic that their properties are size and shape dependent.[1] Observations of growth of 2D materials improves the understanding of their growth processes. This allows for improvements in synthesis and fabrication methods.

The main reason 2D nanomaterials have received so much interest is because they are only a couple of angstrom thick, enabling them to have quantum size effects. [1] Furthermore, 2D nanomaterials have remarkable electrical and optical properties when they are produced as fairly thin layers. This may be the cause of electron confinement effects.

A large group of 2D materials with similar properties was found; the so-called transition metal dichalcogenides (TMDs). A single layer of TMD is typically less than a nm thick, as is to be expected for a 2D material, and can range up to a couple of micrometres. There are two very interesting TMDs, MoS_2 and WS_2, that have surface energies like graphene [8, 9, 10]. WS_2 is more applicable, because it is cheaper and less toxic [6], while it exhibits properties very similar to MoS_2. [11, 12, 13]

WS_2 has some advantages over graphene, namely it is a good light absorber and it has a tunable band gap.[6]. These properties, along with good physiochemical properties make WS_2 a good candidate for (opto)electronics, energy conversion and energy storage.[14].

Understanding the growth of 2D TMDs is important to control the synthesis, fabrication and tailoring of functional properties. Control over the growth of WS_2 can help to tune its properties, in order to improve its application in various fields. WS_2 is formed using thermal decomposition of ammonium tetrathiotungstate (ATT), $(NH_4)_2WS_4$ [15]. The growth process of WS_2 will be examined with in-situ transmission electron microscopy.

Density Functional Theory calculations will be used to explain the findings by comparing the computed lattice parameters to those experimentally obtained for WS_2, WS_3 and WO_3. Furthermore, the energy of each structure will be taken into account to see if the structure is stable. Magnetic properties will also be investigated along with spin-orbit coupling. With this, the band structure will be determined.

2 Theory

2.1 Transmission Electron Microscopy (TEM)

With the help of in-situ TEM experiments, processes like, growth, chemical reactions and physical changes can be observed in real time. Studying these processes can help us understand structure-property relations of the materials being investigated. Studying the growth processes can help us understand how to control the growth parameters. This, in turn, enables us to obtain materials with the desired dimensions and/or size. Characterization of particles by TEM works by transmitting a beam of electrons, through the specimen, to

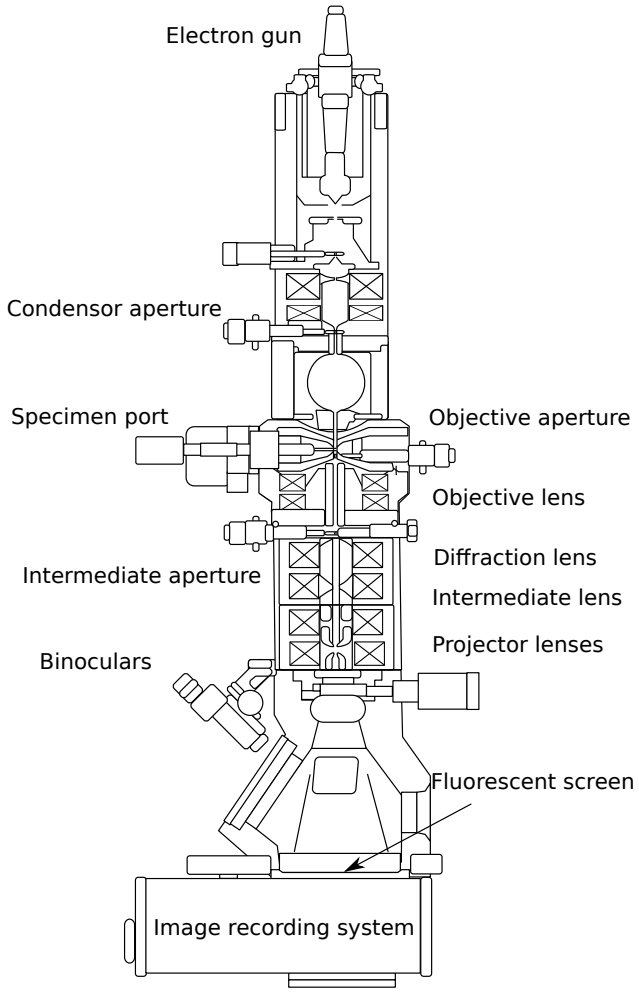

Figure 1: Schemetic representation of a TEM apparatus.[19]

form an image. The TEM has an electron source, consisting of a cathode and an anode, located in the upper part of the microscope. For this experiment a TALOS F200X microscope is used.

In the TALOS F200X, the cathode consists of a tungsten crystal with a ZrO_2 layer surrounding it. With a small positive charge, electrons are pulled out of the tip. These electrons have a very small energy spread, which gives better results. In the TALOS F200X, all the electrons are pulled out of the tip. This means that the electrons that form a beam are going in the direction they are supposed to go, towards the sample. This beam reaches the anode, which has a large positive potential (200KV) and is accelerated towards the sample. This type of cathode is known as a field emission gun (FEG). It gives a coherent energy beam, while still giving highly energetic electrons. The beam is focused by using electromagnetic lenses. [16]

Apertures are used to restrict the electron beam, and are typically used when looking at Bragg reflections to filter out data. The sample is mounted on a mechanical arm, which enables rotation and translation of the sample. The mechanical arm is controlled by the computer attached to the TEM, to allow for small and precise rotations and translations. The projector lenses are used to focus correctly, since we like to see a bit more contrast, it is preferable to take images that are slightly under focused.[17] [16] [18]

TEM has two modes which can be used to analyse the sample, bright-field and dark-field. In bright-field mode the back-ground is white and areas where the sample can be found are dark. The density of the sample

in a given area will determine the darkness of that area. The density refers to both the concentration of the sample as the intrinsic density of the material that is examined. The sample scatters and absorbs a fraction of the incoming electrons which causes the area to appear darker. In bright-field the transmitted beam is used. [20][21]

Dark-field excludes the transmitted electron beam and instead uses the scattered electrons. Dark-field is typically used to enhance contrast, which enables the study of defects in a sample. The distinction between bright-field and dark-field is the location of the objective aperture. To use dark-field, the diffracted beams need to be used. This can be done by using the objective aperture to block the direct beam. [20] [21]

In bright-field TEM, the transmitted electrons are used. These electrons fall on a slide which has patterns on it that allow only certain parts of the electrons beam to pass. The electrons that pass the slide form an enlarged image when they fall on the fluorescent screen. [17] [18] The fluorescent screen is used to find areas worth examining, to find the correct magnification and to see Bragg reflection. Nowadays, the fluorescent screen is typically displayed on a computer monitor. Properties such as density and composition of the material being examined, influence the transmission of the electrons. Since electrons are transmitted through the specimen, it is important for the specimen to be conducting. If the specimen is not conducting, electrons will accumulate, and poor images will be obtained. A schematic representation of the TEM apparatus can be seen in figure 1

Scanning transmission electron microscopy (STEM) is used to take an image of the final state of the nanoparticles. STEM works almost identical to TEM. The difference is that the electron beam is focused to a spot, which then scans the surface of the specimen. Often conventional TEM microscopes also have a STEM mode, just like the TALOS that was used. STEM is used to see the surface of particles. In STEM the electrons that are scattered are collected and this data is used to create the image. For this, a high angle annular dark field (HAADF) detector is used, which collects scattered electrons. This detector collects far more scattered electrons than can pass through an objective aperture.[18]

2.1.1 Heating chip

A heating chip is used to heat the sample while in the TEM. *Wildfire* heating chips, produced by DENSsolutions, have been used. The chip has a viewable area of 850 μm^2 and a 99.5 % temperature homogeneity.[22] This means that all conditions on the chip are similar, which allows for an unbiased examination of the sample. This temperature homogeneity is achieved by a 4-point-probe-measurement. The temperature is controlled by the Joule heating principle of a metal spiral. A current is run through the chip and the resistance produces heat. The 4-point probe enables the use of measured resistance to give a good indication of the temperature.[23]

2.1.2 Drop casting and imaging

Prior to drop casting the 1 % $(NH_4)_2WS_2$ powder dispersed in ethanol onto the heating chip, some preparation steps are required. An argon plasma cleaner has been used to clean the heating chip. By doing so, the heating chip becomes hydrophilic, while it is originally hydrophobic. By using a sonicator bath (BRANSON 1200), the particles in the ATT dispersion are evenly distributed. The ATT dispersion is drop casted onto the heating chip using a Finn pipet, causing the ethanol to evaporate, typically within 5 minutes. This chip is placed in the TEM holder, which is put in another plasma cleaner, to remove the ligands.

Now the chip is ready for examination, it is loaded into the TEM. Before any images can be acquired there are some alignments that need to be performed. The alignments enable us to look at different regions of the sample without going out of focus. We also use the alignments to get the most accurate results possible. The first alignment step is the gun tilt, which is used to maximize the screen current. By doing so, the largest number of electrons reach the area that is being examined. This is followed up by a gun shift to ensure that the beam reaches the area is perpendicularly.

To make sure we do not go out of focus when looking at different regions, another calibration step needs to be done, in which the height of the sample is adjusted. When increasing the temperature above 500 °C the heating chip will exhibit some bulging effects, which causes the sample to shift. This can be corrected for during the measurement. The ideal height is typically a little different for different windows. If necessary, the height calibration can be done again. The final calibration step is to make the FFT rings circular to remove any elongation effects due to astigmatism.

2.2 Energy Dispersive X-ray Spectroscopy(EDX)

EDX is used for both qualitative and quantitative analysis of the sample. The method is based on the detection of X-rays emitted from the sample. The formation of these X-rays is a two-step process. The electron beam hits the sample, which excites some of the electrons or ionizes the atoms in the sample. The atoms will then relax, and the excited electrons will move back into a lower energy shell. The energy difference during this relaxation step can be emitted as X-rays. These X-rays have very specific energy, because the energy depends on the energy difference associated with the shells and can thus be used to identify atoms. [24]
X-rays are a form of electromagnetic radiation which can be detected by silicon drift detectors (SDDs). The SDDs are placed very close to the sample and under an angle. The detectors can calculate the energy of the incoming electromagnetic radiation, and that is how it determines which atom is located at a certain position.[24, 25] This method can also be applied in the TALOS.

2.3 Density Functional Theory (DFT)

2.3.1 Theory

Density Functional Theory (DFT) is a calculation method that is used to find the ground state energy of a system, using the electron density as the main parameter. The full Schrödinger equation should be solved for such calculations, but for systems with many particles these calculations often become tiresome and complex. DFT calculations make some assumptions to simplify the problem.

The first assumption is the Born-Oppenheimer approximation.[26, 27, 28] This assumption fixes all the atoms in place and allows only electrons to move. This is physically like looking at the system at 0 K, which will be done from this point forward. With this assumption the Schrödinger equation simplifies to a Schrödinger equation for electrons. We need to make an additional assumption that will enable us to use the solution for the electrons to describe the total system. To do so, the Hohenberg-Kohn theorems are used. [26, 27, 28]

The first theorem states: *'The external potential $V_{ext}(r)$ is (to within a constant) a unique functional of $\rho(r)$; since, in turn $V_{ext}(r)$ fixes H we see that the full many particle ground state is a unique functional of $\rho(r)$.'*

The second theorem states: *'The functional that delivers the ground state energy of the system, delivers the lowest energy if and only if the input density is the true ground state density $\rho(r)$.*[27]

From the first theorem, it can be concluded that $\rho(r)$ contains information about the wave function, energy, number of atoms and any information about these atoms. This implies that the ground state electron density determines the ground state energy, and all the individual components of the system. It is stated that, 'all properties of all states are formally determined by the ground state density'. The first theorem does not provide us with a method that allows us to directly determine all the properties of the system from $\rho(r)$. The only information that can be gained from this system is for atoms in the ground state. Any information about excited states cannot be obtained from this theory, which is more obvious if the second theorem is also considered. The second theorem is a consequence of the well-known variational principle. Which immediately results in the fact that the system under investigation is in the ground state, since the ground state has the lowest energy.[27, 28] Critical here, is that properties are associated to an external potential.

What is still missing is a good way to account for kinetic energy and the non-classical contributions to the electron-electron repulsion. Typically, these electron-electron repulsion terms are small. The Kohn-Sham approach enables the computation of the kinetic energy to good accuracy. This is done by taking the wave function as a single Slater determinant. This wave function can now be considered as an exact wave function for any system of non-interacting electrons. As simplified as this may be, this solution works for any system. Kohn and Sham went on by calculating as much of the kinetic energy as they could. Any unknown terms were added separately in the form of the exchange-correlation energy. [29, 28] Up to this point, all calculations are exact, and the approximation only appears when the external potential is chosen.

The calculation itself starts out with an initial approximation from which the effective potential is calculated. Next, the Kohn-Sham equation, the one electron Schrödinger equation of non-interacting particles, is solved. The Kohn-Sham equation gives the same density as any given system of interaction particles.[29]. Then, the electron density and the total energy of the system are calculated. Finally, a self-consistency check is done. If the answers are self-consistent, then the calculated values are given as output. Otherwise a new effective potential is calculated.

2.3.2 VASP

All DFT calculations have been done using the Vienna Ab-initio Simulation Package (VASP) version.5.4.1. [30, 31, 32, 33, 34, 35] VASP is a code which performs ab-initio quantum mechanical calculations. It is mainly used for DFT calculations, but it can also be used for post-DFT corrections such as Hartree-Fock or many-body perturbation theory. In order to do these calculations, VASP uses periodic boundary conditions and the electron density is modelled as a superposition of plane waves each having a wave vector k. VASP calculations are either based on Vanderbilt pseudo potentials or on the projector augmented wave method. [36] The projector augmented wave (PAW) method combines both pseudo potentials and the linear augmented-plane-wave method for direct DFT calculations. These calculations are performed with greater computational efficiency. The PAW method is used for ab-initio electronic structures, which will be studied in this thesis. [32] [33]

To start a DFT calculation, VASP requires several input files. The INCAR, POSCAR, POTCAR, KPOINTS and a job file, which calls on an executable. POTCAR files can be obtained from the VASP server, where a catalogue with POTCAR files is provided. POTCAR files describe the pseudo potentials of all atoms in the unit cell. The KPOINTS file contains the k-point grid. The POSCAR contains the information about the atomic positions in the unit cell and the dimensions of the unit cell. In the INCAR file all the settings for the calculation are defined, such as relaxation, magnetisation, etc. In the job file the executable is called on and the number of cores is defined. In this thesis two executables have been used. VASP-O2 has been used for most calculations. Vasp-ncl has been used for the non-collinear spin-orbit coupling calculations.

After the calculation is finished VASP provides multiple output files. Output files used in this thesis are the OUTCAR, CONTCAR, OSZICAR, EIGENVAL and DOSCAR.
The OUTCAR contains the information about the calculation. In it most values, such as the total magnetic moment and the fermi-energy, can be found. This file also contains warnings and errors whenever something is wrong in the input files. The CONTCAR is similar to the POSCAR. When a relaxation calculation is performed the CONTCAR provides the relaxed unit cell, which can be used in further calculations. In the OSZICAR the energy of the structure can be found, along with the energy difference between the previous iteration. This file is used when examining the energy of structures. In this thesis it will be used to determine the stability of WS_3 and WS_2. The EIGENVAL file contains the energy for the electron bands at each k-point. This file is used for making band structures. Finally, the DOSCAR file contains the density of state as a function of energy. VASP provides several more output files, but these were not used in this thesis.

2.3.3 Method

The stability of WS_2, WS_3, S and WO_3 will be investigated with DFT calculations. Depending on how large the cut-off energy (ENCUT) and the k-point spacing is, the best values to maintain high-accuracy

DFT calculations will be determined. Larger values for ENCUT k-point spacing yield more accurate the DFT calculations. These higher accuracy calculations require more computational power, making them less favourable. What will be investigated here is what the lowest possible settings are, that still provide accurate results. The results may deviate ±0.5 meV/atom from the reference value. This is a process known as benchmarking.

The benchmarking procedure followed is setting the ENCUT value to 900 and decreasing the values by 100 each time. Similarly, for the k-point spacing, which will be decreased by two for the smallest number and the other values will be changed accordingly. When the energy is being optimised the highest k-point spacing will be used. When the k-point spacing is being optimised ENCUT is kept at 900.

2.3.4 K-point spacing

The k-point spacing is typically referred to as the reciprocal space. This has dimensions of $[\frac{1}{m}]$. We are primarily looking at 2 structures, WS_2 and WO_3, which are hexagonal and square respectively. To properly determine the k-point spacing, the distances in real space have to be taken into account. Due to the inverse relations, small lattice parameters in real space are large in k-space and vice versa. The input lattice parameters for WS_2 are given below:

$$\begin{pmatrix} 3.190731 & 0.000000 & 0.000000 \\ -1.595365 & 2.763254 & 0.000000 \\ 0.000000 & 0.000000 & 14.202402 \end{pmatrix}$$

Here the diagonal is considered as being 8,8,2 in k-space. 8,8,2 Will be denoted as k2. Multiplying each component with 2 would give k4, etc. Based on the lattice parameters, this structure is hexagonal.

The input lattice parameters for WO_3 are given below:

$$\begin{pmatrix} 3.863000 & 0.000000 & 0.000000 \\ 0.000000 & 3.863000 & 0.000000 \\ 0.000000 & 0.000000 & 7.725000 \end{pmatrix}$$

Here the diagonal is considered as being 4,4,2 in k-space. 4,4,2 Will be denoted as k2. Multiplying each component with 2 would give k4, etc. Based on the lattice parameters, this structure is cubic.

2.3.5 Van der Waals functionals

After the optimal ENCUT and k-point values have been determined, a van der Waals functional is applied to account for van der Waals attractions between atomic layers. Here, two different van der waals functionals will be compared with the generalised gradient approximation that has been used up to now. The generalized gradient approximation of Perdew, Burke and Ernzerhof (GGA-PBE) mainly incorporates short-range interactions. [34] Since van der Waals is a long range interaction this is not modelled very well. [37] [38] [39] [40] [33]

The first functional, is the DFT-D3 correction of Grimme. This functional includes atom-pairwise specific dispersion coefficients which are used to describe the van der Waals interactions. [41] [39] [42] [40]

The second functional, is the van der Waals correction of Dion (optB88-vdW). This functional includes non-local contributions for the correlation energy term. Its main application is for layered geometries to contain long-range forces in the correlation term. The long-range force we are interested in is the van der Waals force. Therefore, this functional could give us some insight in the effect of this force on the structure.[42] [43] [39] [40] [37]

2.3.6 Spin-orbit coupling (SOC)

When looking at systems with heavy elements, spin-orbit coupling effects can be observed. Spin-orbit coupling describes the interaction between the electrons spin and its orbital motion around the nucleus. [44] An electron moving in an external electric field experiences a magnetic field in its frame of motion. Therefore,

movement of electrons causes a shift in the electrons energy levels, which in turn leads to energy band splitting. This shift is a result of the electromagnetic interaction between the spin of the electron and the electric field that surrounds the nucleus. [44]

The external field depends on the orientation of the magnetic moments [45], because of this dependence the final spin-orbit coupling depends on the initial magnetic moments of the material. A system which has weak intrinsic spin-orbit coupling, like graphene, can be applied in spin-based devices. Having weak intrinsic spin-orbit coupling ensures that spin propagates coherently. [46] The main consequence of spin-orbit coupling is energy band splitting, which allows for possibilities in fields such as spintronics. [45]

The effect of SOC should be small for a defect free WS_2 structure, according to Li [47]. It is stated that a defect of W possesses a magnetic moment of 2 μ_B, similar to what will be simulated in this thesis.

3 Results

3.1 TEM results

ATT was pipetted onto the heating chip. ATT gives an amorphous structure at room temperature and will start to show lattices after it undergoes a transformation. During this transformation, sulphur and ammonium leave the composition, causing WS_2 to form. This implies that, at room temperature, most areas appear as amorphous. What is remarkable is that at room temperature, a lot of vertically grown sheets are present. Increasing the temperature to 50 °C does cause, to some extent, growth of these vertically grown sheets. The average amount of layers is increased from two or three to five. This could be an indication that the vertical sheets are stable.

We will now distinguish between samples that were drop casted onto the heating chip shortly after preparation and those that were kept in ethanol for more than one week. The latter will be referred to as contaminated from this point onward. Keeping the samples in ethanol normally does not affect the material. However, in this case we did notice some changes. First, the samples that were kept in ethanol for longer became whiter, whereas the newly prepared samples were yellow. ATT is orange to yellow in colour, indicating that a reaction has occurred when the solution becomes whitish. Secondly, the lattices in these samples appear at a lower temperature. The samples that have been kept in ethanol start showing lattices after being heated to 50 °C. Whereas, in samples that have been drop casted shortly after preparation, lattices appear at 150-200 °C. Finally, there are two types of lattices that appear in the contaminated sample, namely square and hexagonal lattices.

The first structures that became visible were the vertically grown sheets. The vertically grown sheets could already be observed at room temperature, where they consisted of, on average, two to three layers with an average spacing of 0.62 nm. At room temperature the vertically grown sheets were small in the lateral directions, with a size of, about, 5 nm. Heating to 50 °C seemed to have the biggest effect on the structure of the vertically grown sheets. The vertically grown sheets now consisted of five layers on average, and lateral distances had doubled to 10 nm. Increasing the temperature further did not have any drastic effects on the size or number of layers of the vertically grown sheets. After increasing the temperature further, we saw that the average number of sheets slowly increased. At 500 °C the average number of sheets was eleven, which is significantly higher than at 50 °C. Looking at even higher temperatures, it could be observed that the vertically grown sheet still increased in size. At 650 °C very large vertically grown sheet were found, see figure 2. For different areas the size does vary a little, which explains why the vertical sheets look a little smaller at 700 °C.

The lateral distances of the vertically grown sheets varied between 2 nm to 10 nm in the temperature range that has been examined. The amount of vertically grown sheets also varied greatly. In some regions, the vertically grown sheets were visible over the entire area being examined, whereas in other regions the vertically grown sheets were barely, if at all, present. Initially, it was thought the growth of the vertically grown sheets of WS_2 was a beam induced effect. At room temperature the vertically grown sheets only seemed to appear at areas that were examined. Oddly enough, most growth occurred in areas where some

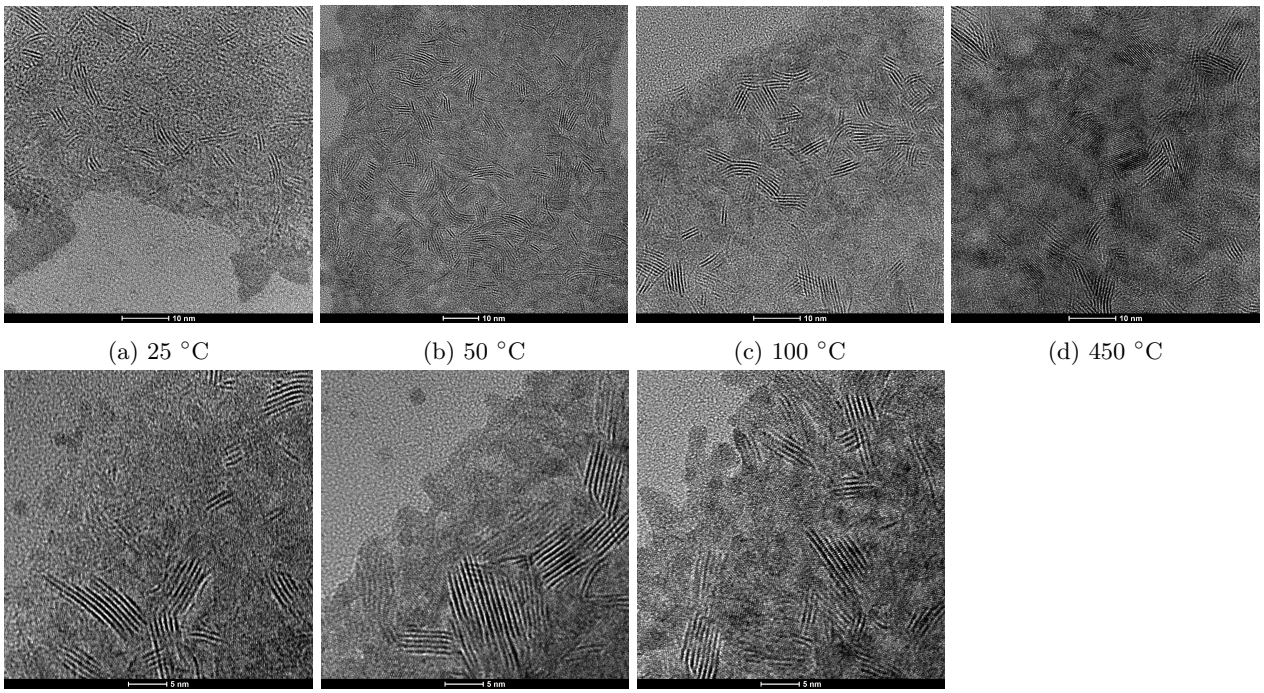

(a) 25 °C (b) 50 °C (c) 100 °C (d) 450 °C

(e) 500 °C (f) 650 °C (g) 700 °C

Figure 2: Vertically grown sheets for different temperatures, within the temperature range the sheets exhibit growth.

vertically sheets had already been seen. When the area was examined, not much growth was seen, whereas revisiting an area typically did show some growth.

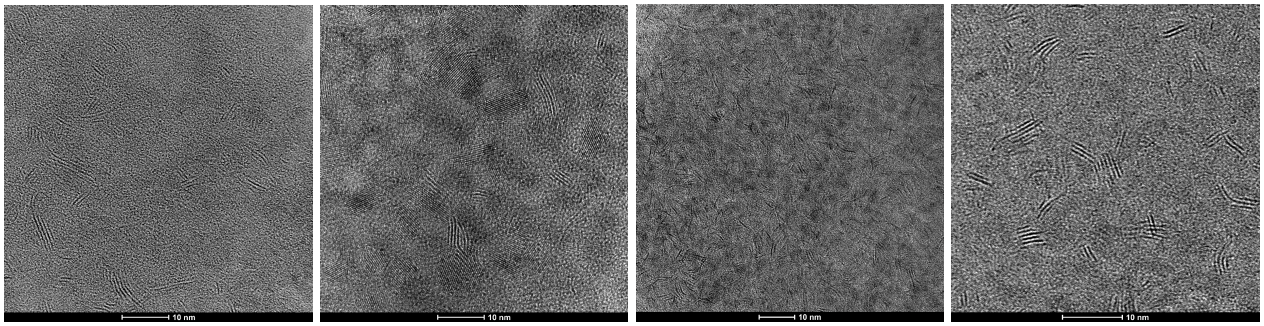

(a) 25 °C (b) 300 °C (c) 350 °C (d) 400 °C

Figure 3: Vertically grown sheets for different temperatures, acquired in the middle of the sample.

This explanation was disproven when the vertically grown sheets were also observed in another window of the heating chip at 450 °C, which had not been studied before. The vertically grown sheets found in both windows were comparable in size and number of layers.

The vertically grown sheets were observed in areas of dense ATT precursor. Growth was monitored at the edges in order to obtain better images. Due to high precursor concentration in the middle, it is hard to see large vertically grown sheets in this region, see figure 2 . Compared to figure 3, the vertically grown sheets are further away from edges. As can be seen this was impactful on the observable size of the sheets. This indicates that the edges are more suitable for the study of vertically grown sheets.

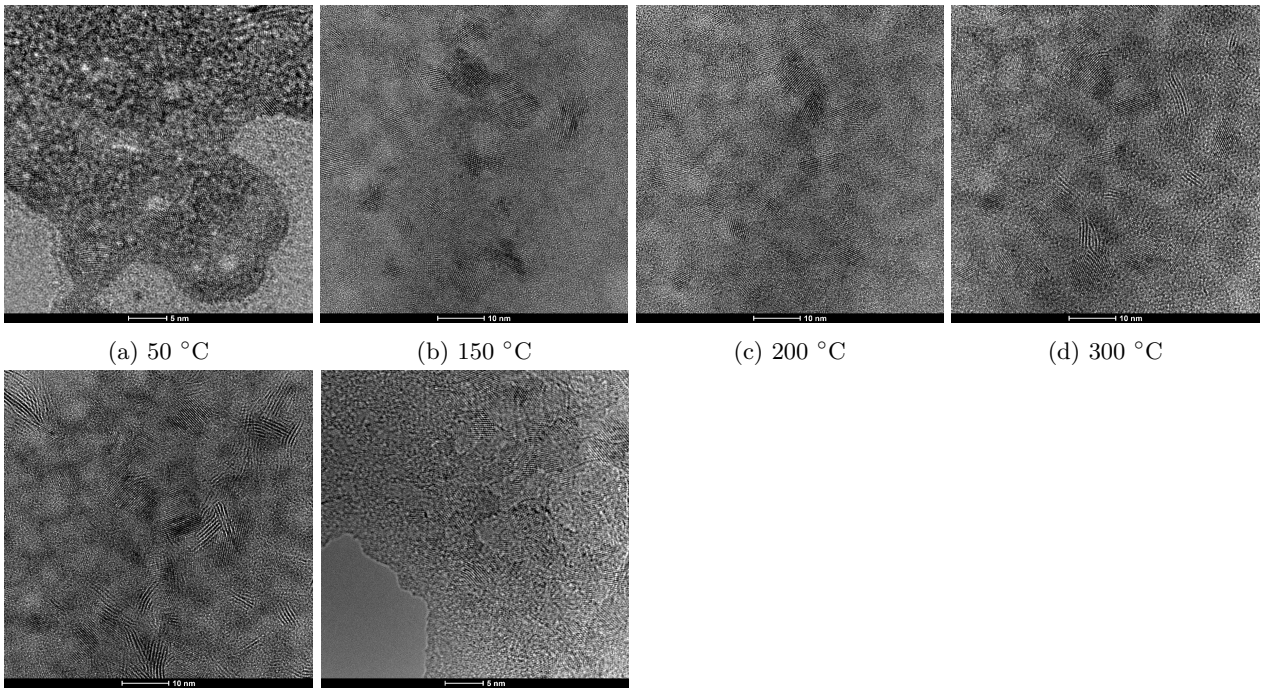

(a) 50 °C (b) 150 °C (c) 200 °C (d) 300 °C

(e) 450 °C (f) 800 °C

Figure 4: (a)-(e): Square lattices for different temperatures. (f) Hexagonal lattices in the contaminated sample.

The next thing we found were square lattices. These first appeared at 50 °C, at which point they were still very small and hard to examine. Increasing the temperature to 100-150 °C enabled us to examine these lattices. The square lattices were only visible in ATT that had been kept in ethanol for a longer period of time. This is the main reason we believe this structure to be WO_3. Examining the lattice parameters at 150 °C gives us an interatomic spacing of 0.37 nm. The literature value for WO_3 is 0.38 nm.[48] This means that this could indeed be a WO_3 lattice. This structure is further investigated with DFT calculations to see if the WO_3 structure is stable.

At 300 °C, the square lattices are about 10-15 nm in the lateral direction, see figure 3b. Increasing the temperature of these samples causes an increase in quantity of square lattices. At 450 °C the number of lattices is significantly higher than at 50 or even 150 °C. Furthermore, the square lattices are also better defined at 450 °C than they were at 150 °C, see figure 4. The square lattices were only seen in the contaminated samples. In the uncontaminated samples, the square lattices were only observed when a lattice transition occurred.

The first WS_2 structures that will be treated in this thesis, were found in the contaminated sample. Hexagonal structures were visible at 50 °C. In this case, all the hexagonal lattices were small in the lateral directions. Increasing the temperature gave more order within the lattices and their size in the lateral directions increased. Where at 50 °C, the size in the lateral directions was in the range of 1-2 nm, this had increased to 5 nm at 300 °C. These can be see in figures 3a and at the bottom of figure 3d At 700 °C the lateral size had increased to 10 nm, see figure 2g. Faceting occurred at 800 °C for the lattices that were still around 5 nm in size, see figure 4f. In this figure the faceting is a bit hard to see, but the edges of each lattice do lean more towards a faceted orientation now than they did at a lower temperature. The inter planar spacing of WS_2 here is 0.32 nm, which agrees with the literature value of 0.315 nm.[11]

The WS_2 in the uncontaminated sample followed a slightly different growth process than in the contaminated sample. The vertically grown sheets grew the same for both samples, but the lattices themselves had significant differences. The first time the WS_2 hexagonal lattices became visible was at 150 °C. The lattices had a lateral size of about 2-3 nm, and a lattice spacing of 0.32 nm. After the temperature was increased to 200 °C, more small lattices formed. The lattice size had not increased significantly at this point. Having increased the temperature further to 300 °C, the lateral size increased and the number of lattices also increased. The lateral size has increased to, on average, 5 nm. At 450 °C, the lattice started to show faceting, which was only observed after annealing at 450 °.

At this point, the lattices were also significantly larger in the lateral directions, compared to samples that were annealed at 450 °C. Now the sizes that could be observed were in the range of 10-15 nm. Increasing the temperature more quickly enabled us to observe these processes as they occurred. Increasing the temperature to 650 °C, allowed us to study the formation of lattices in the regime from 300-650 °C. The lateral sizes increased, from the aforementioned 5 nm, to 10-15 nm. After increasing the temperature to 800 °C, processes such as oriented attachment, coalescence, lattice matching and faceting could be observed, see appendix B.

Furthermore, at high temperatures, e.g. 800 °C, other aspects of the WS_2 lattice could be studied. We could, for example, study two overlapping lattices, since they are distinguishable now. Over the entire temperature range, the lattice parameter remains, on average, 0.32 nm. Several lower lattice parameters were found, these were typically a factor $\sqrt{2}$ lower, meaning that the sample was being examined through a different facet.

Processes such as lattice matching, faceting and oriented attachment allow us to study the growth processes that WS_2 undergoes. These processes enable us to grow larger lattices and allow us to create material with desirable dimensions. At 800 °C these processes can be studied. However, some of these processes already occur at 450 °C.

Faceting allows us to obtain the desired dimension of our sample. Heating the sample to 450 °C will be enough for this process to occur. Oriented attachment has not been observed at lower temperature, the main energy penalty here is associated with bringing two lattices close together. This is why oriented attachment has not been observed at lower temperatures. Lattice matching can occur at most temperatures, which is why the lattice parameters increase in the lateral directions for a large temperature range.

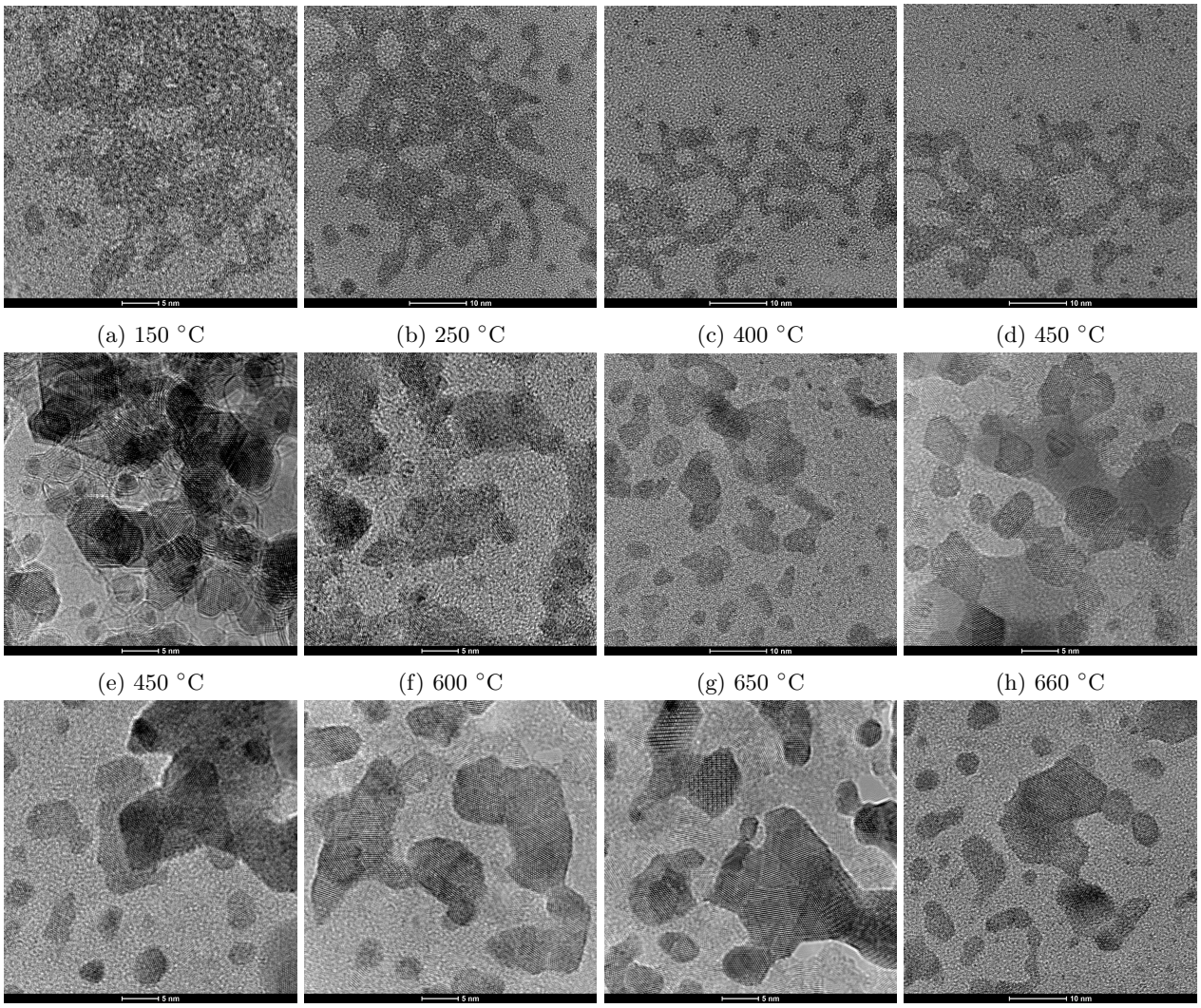

(a) 150 °C (b) 250 °C (c) 400 °C (d) 450 °C

(e) 450 °C (f) 600 °C (g) 650 °C (h) 660 °C

(i) 800 °C (j) 800 °C (k) 800 °C (l) 850 °C

Figure 5: Hexagonal lattices as a function of temperature. (e) Annealed at 450 °C for 30 min, which resulted in faceted lattices at a lower temperature.

3.2 EDX results

EDX has been used to determine the concentration of tungsten and sulphide in the samples after they were heated to 650 °C and 850 °C. After the samples were heated to 650 °C, we found that the samples contained 37-40 % and 60-63 % for tungsten and sulphur respectively. Whereas in another region 54-56 % and 44-46 % for tungsten and sulphur were found respectively. In every measurement the uncertainty for tungsten is relatively high, around 23 % for a low tungsten concentration and 26 % for a high tungsten concentration. On the other hand, the uncertainty for sulphur is low, about 1 %. We found a ratio of approximately 1:2 for W:S. This means that, we are looking at WS_2 at 650 °C. There are some exceptions, where a 1:1 ratio of tungsten to sulphur was found. These difference are a result of the region that was examined. The 1:2 ratio was found by examining a region containing a larger number of lattice than the region where a 1:1 ratio was found.

After having heated the sample to 850 °C, we saw that the samples still contained about 41-44 % and 56-59 % for tungsten and sulphur respectively. There was also an area where the tungsten concentration was 57 %, while the sulphur concentration was 43 %. We did, however, also do quantification measurements where nitrogen, oxygen and silicon were included. This gave a tungsten concentration of 8 %, while sulphur had a concentrations of 10 %. At this point, we also needed to take into account that WS_2 can transition to a metal tungsten composition. This ratio is approximately 1:1, meaning that metallic tungsten is probably being produced at this point.

Including nitrogen, oxygen and silicon decreases the quantity of both tungsten and sulphide drastically, but it does not have any real impact on the ratio between them. This means that regardless of whether we include N, O and Si, we find approximately the same results. Therefore, we do not necessarily have to include these other elements in the EDX results. We have not done any EDX on contaminated samples, since WS_2 is the main focus of this thesis. A ratio of approximately 1:2 for W:S has been found. From this it is concluded that WS_2 has formed at 650 °C.

3.3 DFT Results

3.3.1 Van der Waals functionals

After the benchmarking had been completed, the van der Waals functionals were tested. The benchmarking results can be found in appendix A. Van der Waals functionals were tested by running them and seeing which functional produced a unit cell that held the closest resemblance to the reference values for this composition.

Table 1: WO_3 van der Waals functionals. The reference unit cell is used to compare the three functionals.

Reference unit cell		GGA-PBE		DFT-D3		optB88-vdW	
Direction	Reference (Å)	Distance (Å)	Diff (%)	Distance (Å)	Diff (%)	Distance (Å)	Diff (%)
a	3,65	3,83	5,0	3,83	4,8	3,83	5,0
b	3,77	3,83	1,8	3,83	1,6	3,83	1,8
c	7,68	7,67	-0,15	7,65	-0,35	7,67	-0,16

Table 2: WS_2 van der Waals functionals. The reference unit cell is used to compare the three functionals.

Reference unit cell		GGA-PBE		DFT-D3		optB88-vdW	
Direction	Reference (Å)	Distance (Å)	Diff (%)	Distance (Å)	Diff (%)	Distance (Å)	Diff (%)
a	3,15	3,19	1,1	3,17	0,57	3,19	1,3
b	2,73	2,76	1,1	2,75	0,57	2,77	1,3
c	12,3	14,1	14	12,4	0,91	12,5	1,7

From tables 1 and 2 it becomes clear that the DFT-D3 functional gives the best results. This gave a unit cell that has the most resemblance to the reference unit cell. Therefore this functional was used for further

Table 3: Results from DFT-D3 calculations for WS_2, WS_3, WO_3 and S.

Structure	WS_2	WS_3	WO_3	S
Energy (eV/atom)	-8,13	-6,53	-9,21	-4,24
a	3,17	4,66	3,83	10,64
b	2,75	4,66	3,83	13,01
c	12,4	8,33	7,65	24,80

Table 4: Lattice values and energies for different magnetic samples

sample	ref	AFM2	AFM4	FM2	FM4
total magnetic moment	0	0	0	0	0
a	3,15	3,17	3,17	3,17	3,12
b	2,73	2,74	2,75	2,75	2,70
c	12,3	12,4	12,4	12,5	10,3
E0	-48,8	-48,8	-48,8	-48,8	-45,4
ΔE (meV/atom)	0	0,13	-0,0005	0,008	570

calculations. With the DFT-D3 functional the energies of WS_2, WS_3, WO_3 and S have been calculated. The lattice parameters that were found from these calculations have been compared with the experimental results.

Comparing the results of table 3 with the literature values mentioned in section 3.1, it can be seen that WS_2 and WO_3 structures are the most similar to the experimental lattice parameters. WS_2 has a close resemblance to the hexagonal lattices and WO_3 has a close resemblance to square lattices. Since all structures containing sulphur were run using the same ENCUT value and k-point spacing (scaled when necessary) the energy of these structures can be compared. From this we can conclude that WS_3 is unstable compared to the WS_2 and S during a transition. $WS_3 \rightarrow WS_2 + S$ gives 2,5 eV per WS_3 that is converted. Hence WS_3 is energetically far less favourable than WS_2 and will likely not form. The lattices that are formed are WS_2 and WO_3 for hexagonal and square lattices respectively. For these structures, the computed parameters match those that have been experimentally found.

3.3.2 Magnetisation

All calculations up until now were for non-magnetic tungsten. Since the calculations are based on a defect free sample, this is a good approximation. When magnetic effects are taken into account however, the magnetism should converge to zero for each calculation, if it is indeed non-magnetic.
Calculations have been done for both anti-ferromagnetic and ferromagnetic samples. For each sample, two different magnetic moments of 2 and 4 μ_B were considered. This indicates the strength of the magnetism on the tungsten atoms.

For each calculation, the magnetic moments on all atoms converged to zero and most samples converged to approximately the same unit cell as the non-magnetic sample, see table 4. The exception being the ferromagnetic WS_2 with 2 μ_B, which got trapped in a local minimum. This might have been caused by the magnetic properties of this sample. Since its energy is much higher than the real minimum, this state will never exist.

3.3.3 Spin-Orbit Coupling (SOC) and bandgaps

SOC effects were investigated to see if energy band splitting occurs. Based on fig 6, it can be interpreted that SOC plays a significant role. The maximum density for a given energy does not exceed ten without SOC. If SOC is included, however, the maximum density exceeds twenty. This is twice as large. The maxima do not appear at the exact same energies, but deviate between 0.01-0.06 eV. These calculations were done on defect free samples, which already minimizes the intrinsic effect. Given that WS_2 does not display significant SOC

effects, in the sense that the energy of each point remains the same, it might not be applicable for spin-based devices.

Including SOC does not change the fermi-energy. Density of state plots for different initial magnetic moments can be found in figure 11 in Appendix C. From these density of state plots, it can be seen that a ferromagnetic structure causes a more significant change in the density of states. The underlying reason may be, because in the ferromagnetic structure, the fermi-energy is located at a different position.

Since we are doing calculations on defect-free WS_2, we expect the influence of SOC to be small. Based on the results it can be concluded that this is indeed the case. The presence of defects should have a larger impact on the DOS and spintronic effects, as was found in the paper by Fang [47].

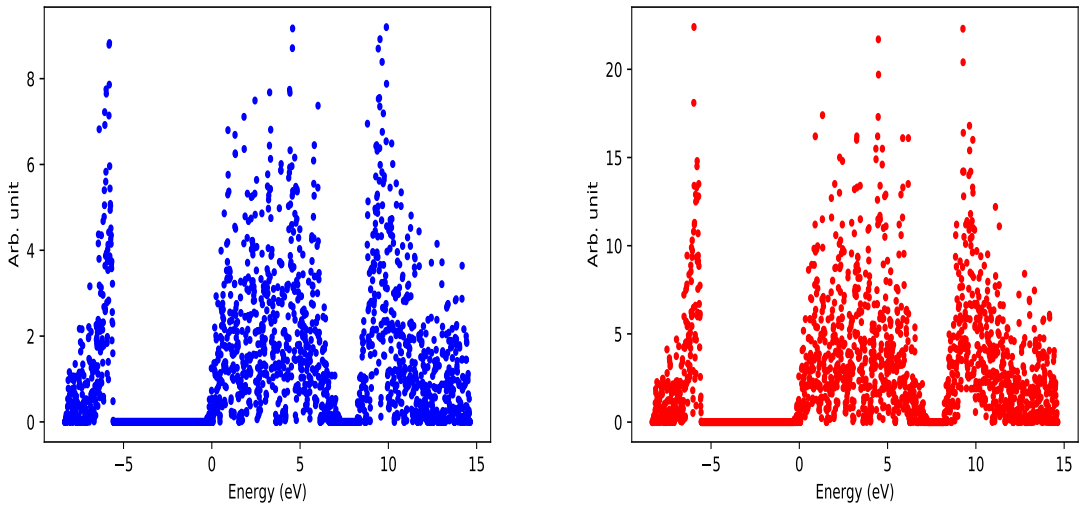

(a) Without SOC (b) With SOC

Figure 6: Density of state plot for WS_2, with and without SOC.

DFT calculations where magnetism had not been included, had a band gap of 1.638 eV, see table 5. Activating an electric field that results in a magnetic field will cause a change in the band gap.

VASP typically overestimates band gaps. The band gap of WS_2 is 1.32 eV according to literature. [49] From this it can be observed that the initial magnetic moment influences both the fermi-energy and the band gap. By comparing the calculations with SOC, it becomes clear that in these calculations SOC causes a decrease in the band gap of 46 meV for both the AFM structures.

In the FM structure, the fermi-energy has increased to two times that of the non-magnetic structure and the band gap has completely disappeared. There is an overlap of 171 meV when SOC is not taken into account, and an overlap of 140 meV when SOC is taken into account. The bands that cross the fermi-level are both spin up and spin down, see figure 12h in appendix D. Since both the spin up and spin down states cross the fermi-energy, WS_2 is a conductor. The same result was found for the DOS for the spin up state and the spin down state, which were completely overlapping. The band structures can be seen in Appendix D.

WS_2 has a tunable band gap, depending on the strength of the electric field that is applied, the band gap can, to some extent, be controlled. The fact that the band gap is tunable could make it more applicable than graphene in some situations. The tunable band gap makes WS_2 suited for semi-conductor applications.

Table 5: Indirect band gaps and fermi-energies for different magnetic WS_2 samples. $\vec{m}$ is used to indicate the initial magnetic moment

Magnetic property	Fermi energy (eV)	Band gap (eV)
non-magnetic	5.156	1.638
AFM, $\vec{m} = 2\mu_B$	7.757	0.992
AFM, $\vec{m} = 2\mu_B$, including SOC	7.757	0.948
AFM, $\vec{m} = 4\mu_B$	7.657	1.022
AFM, $\vec{m} = 4\mu_B$, including SOC	7.657	0.976
FM $\vec{m} = 4\mu_B$	10.746	0
FM, $\vec{m} = 4\mu_B$ including SOC	10.746	0

4 Discussion

Many different properties of WS_2 have been investigated. This thesis now provides a general overview of the properties of WS_2. However, several of these properties can be investigated in more detail.

The exact reason for the formation of vertically grown sheets remains unknown. In order to produce a sample with the desired dimensions, it might be advantageous to also know what causes the growth of vertically grown sheets. These sheets break the 2D symmetry in the sample, making them undesirable. At higher temperatures the vertically grown sheets are typically not found within a faceted lattice, making their presence not as problematic. In order to see if the vertically grown sheets are a result of beam effects, an ex-situ sample could be heated to a similar temperature and then examined in the TEM. The vertically grown sheets should still be present if they are not beam induced.

Initially, WO_3 was not expected to be found, that is why it is referred to as the contaminated sample. The reaction between ethanol and tungsten was unexpected. Some DFT calculations have also been done on WO_3 to see if this could verify why the square lattices were found. It is, however, good to take into account that the ATT should not be kept in ethanol for a longer period of time for future experiments, since it influences the results.

WO_3 also has a hexagonal structure, however this has a lattice parameters of 0.3625 nm [50]. This is slightly higher than the hexagonal lattices parameters of WS_2. This structure has, however, not been investigated, while it could have been present in the contaminated sample. Perhaps not all the hexagonal lattices were WS_2 in this structure. This hexagonal WO_3 has also not been investigated with DFT. Main reason being that WO_3 is an contamination and not the material of interest nor the focus of this thesis.

Overall, the investigation of different lattices types is detailed enough. Temperatures at which different structures are formed and at which the lattices organise themselves have been found. There are also some samples that were annealed at lower temperatures. This also shows that these processes occur at lower temperatures, but at a slower rate. Based on these findings, the most efficient method can be found to produce the desired dimensions.

The examination of the quantities of W and S with EDX confirmed that the lattice that had been found was indeed WS_2. This additional method provided additional information, to help determine the lattice. In addition, at higher temperatures this method showed that a tungsten crystal starts to form. This taught us that heating to even higher temperatures will not be beneficial.

All DFT calculations have been performed at 0 K. As a result, the energy gained by the formation of WS_2 from WS_3 might differ when calculated at room temperature. However, it is very unlikely that WS_3 will become more stable than WS_2 at higher temperatures.

Magnetic properties are found to influence the band gap. If a relaxation is done, the magnetic moments of WS_2 converge to zero. However, when WS_2 is forced into an magnetic configuration, the band gap changes based on the results in table 5. Ideally multiple magnetic moments are investigated to look for a relation, if it exists, between the magnetic moment and the band gap. This would allow for control over the band gap. What is odd is that the ferromagnetic WS_2 has a small overlap in bands. The bands never intersect, but this might be an area of interest for further research.

A FM calculation with an initial magnetic moment of 2 μ_B was supposed to be included for the band structures and SOC. However, this calculation took significantly longer to run. It was seen from previous calculation that this gave results that ended in a local minimum. This might be why these calculations took such a long time to complete, and it could make them less viable since they may not represent the true ground state of the structure.

5 Conclusion and outlook

Many different aspects of WS_2 have been studied. Magnetic properties have an influence on the band gap, which means that the band gap can be controlled by using an external electric field. When the system is relaxed the magnetic moments converged to zero. WS_2 can be formed with ATT and it forms faceted lattices at 450 °C, while the lattices grow within the region of 100 - 800 °C. With EDX a ratio of approximately 1:2 for W:S was found at 650 °C indicating that it is stable at 650 °C.

The temperature range within which WS_2 forms is useful for making a WS_2 lattice with the desired dimensions and the earlier samples that were contaminated taught us that the ATT solution needs to be drop casted shortly after preparation to obtain good results for WS_2.

Each of these results is applicable in a different way. From the results it became clear that WS_2 is not applicable for magnetic purposes, as its magnetic moments converge to zero. When the system is forced to adopt a magnetic configuration the band gap can be changed, making WS_2 suitable for semi-conductor applications. SOC has minimal effects on the DOS, defects would allow there to be more spintronic effects. SOC did, however, have a small effect on the band gap.

With these results, several fields where WS_2 can be applied have been found, and in several situations it could be a viable alternative to graphene. Further research can be done on the conductive properties of WS_2, along with more different magnetic moments to control the band gap further. The results from this thesis show that the band gap of WS_2 changes for different magnetic moments. If the band gap can be accurately controlled, WS_2 could find many applications within the semi-conductor field.

References

[1] Seal S. Gupta A. Sakthivel T. "Recent development in 2D materials beyond graphene". In: *Progress in Material Science* 73 (Mar. 2015), pp. 44–126.

[2] Swart I. *Structure of Matter. lecture notes 2018-2019*. Graphene. reader. Utrecht University Debye institute for Nanomaterials Science, 2018. Chap. 3, pp. 65–71.

[3] Hall H.E. Hook J.R. *Solid State Physics*. 2 (corrected). The Atrium, Southern Gate, ChiChester, West Sussex PO19 8SQ, England: John Wiley & Sons, 2010. Chap. 1, pp. 41–47. ISBN: 9780471928058.

[4] *Graphene Applications: what is graphene used for?* Tech. rep. 1. 9 Har Tsin St. Kfar Saba, 4430809 Israel: MetalGrass LTD, Dec. 2019.

[5] Li Z. Wang J. Zhang J. Li X. Li X. "WS_2 nanoflakes based selective ammonia sensors at room temperature." In: *Sensors and Actuators* 240 (Aug. 2016), pp. 273–277.

[6] ACS materials LLC. *Graphene-like Materials*. ACS Materials. Dec. 2017. URL: `https://www.acsmaterials.com/blog-detail/graphene-like-materials.html`.

[7] Patil P.S. Sadale S.B. "Synthesis and characterization of type-II textured tungsten disulfide thin films by vdWR process with Pb interfacial layer as texture promoter". In: *Journal of Crystal Growth* (Jan. 2006), pp. 363–368.

[8] O'Neill A. Bergin S.D. King P.J. Khan U et al Coleman J.N. Lotya M. "Two dimensional nanosheets produced by liquid exfoliation of layered materials". In: *Science* (2009). This source gives the energies of WS2., pp. 568–571.

[9] Vega A. Díaz E. Ordóñez S. "Adsorption of volatile organic compounds onto carbon annotubes, carbon nanofibres, and high-surface-area graphites." In: *Journal of Colloid Interface Science* (2007). This source gives the energies of graphene., pp. 7–16.

[10] Cucinotta C.S. Sanvito S. Bergin S.D. Mezel R. et al. Cunningham G. Lotya M. "Solvent exfoliation of transition metal dichalcogenides: dispersibility of exfoliated nanosheets veries only weakly between compounds." In: *ACS Nano* (2012). This source gives the energies of WS2., pp. 8983–8999.

[11] Jellinek F. Schutte W.J. De Boer J.L. "Crystal structures of tungsten disulfide and diselenide". In: *Journal of Solid State Chemistry* 70 (Feb. 1987), pp. 207–209.

[12] Chang X. Sun S. Li Z. "Synthesis and structural characterization of tungsten disulfide nanomaterials". In: *Materials Letters* (July 2011), pp. 3164–3166.

[13] Mkhoyan K.A. Wu R.J. Odlyzko M.L. "Determining the thickness of atomically thin MoS_2 and WS_2 in the TEM". In: *Ultramicroscopy* (June 2014), pp. 8–20.

[14] Cheng Y. Cheng F. Wang L. Liu N. Li L. Su J. Gao Y. Zhang Y. Zhang Z. "In situ TEM observations of controlled growth of two-dimensional WS_2 with vertically aligned layers and high-temperature stability." In: *Nano Energy* (Nov. 2019). This paper is the one that intially found the vertically grown layers which we also found, and they did some further research on these., pp. 1–8.

[15] Szilágyi I.M. Hunyadi D. Ramos A.L.V.M. "Thermal decomposition of ammonium tetrathiotungstate". In: *Journal of Thermal Analysis and Calorimetry* (Feb. 2015), pp. 209–215.

[16] Reimer L. *Transmission Electron Microscopy*. 1st ed. Physikalische Institut, Westfälische Wilhelms-Universität Münster, Domagkstraße 75, D-4400 Münster, Fed. Rep. of Germany: Springer-Verlag Berlin Heidelberg GmbH, 1984. Chap. 1, pp. 1–5. ISBN: 9783662135556.

[17] Atomic World. *Principle of TEM*. The Chinese University of Hong Kong. URL: `http://www.hk-phy.org/atomic_world/tem/tem02_e.html`.

[18] Reimer L. *Transmission Electron Microscopy*. 1st ed. Physikalische Institut, Westfälische Wilhelms-Universität Münster, Domagkstraße 75, D-4400 Münster, Fed. Rep. of Germany: Springer-Verlag Berlin Heidelberg GmbH, 1984. Chap. 4, pp. 86–133. ISBN: 9783662135556.

[19] Gringer. *Commons: Scheme TEM en.png*. This is the image that displays the TEM. Jan. 2009.

[20] Reimer L. *Transmission Electron Microscopy*. 1st ed. Physikalische Institut, Westfälische Wilhelms-Universität Münster, Domagkstraße 75, D-4400 Münster, Fed. Rep. of Germany: Springer-Verlag Berlin Heidelberg GmbH, 1984. Chap. 6, pp. 186–193. ISBN: 9783662135556.

[21] *TEM: Bright field versus dark field*. URL: https://chem.libretexts.org/Courses/Franklin_and_Marshall_College/Introduction_to_Materials_Characterization_-_CHM_412_Collaborative_Text/Electron_and_Probe_Microscopy/TEM%3A_Bright_field_versus_dark_field.

[22] DENSsolutions. *The revolutionary Wildfire Nano-Chip*. DENSsolutions. URL: https://denssolutions.com/products/wildfire/nano-chip/.

[23] Pivak Y. *Product Brochure Wildfire*. This is the brochure about the heaitng chip. DENSsolutions.

[24] *How does EDX Analysis with a Scanning Electron Microscope (SEM) work?* Jan. 2020. URL: https://www.azom.com/article.aspx?ArticleID=16256.

[25] *Scanning Electron Microscopes*. ThermoFisher Scientific, 2020.

[26] Gog H. "Thermische stabiliteit van tweedimensionale magaanoxides. DFT-berekeningen". Dutch. In: *Nederlands Tijdschrift voor Natuukunde* (Mar. 2019), pp. 21–23.

[27] Holthausen M.C. Koch W. *A Chemist's Guide to Density Functional Theory*. 2nd ed. Varrentrappstraße 40-42 D-60485 Frankfurt Germany, Hans-Meerwein-Straße D-35032 Marburg Germany: Wiley-VCH, 2008. Chap. 4, pp. 33–37. ISBN: 9783527303724.

[28] Gupta S.S. *Single Atoms, Molecules, and Sub-Nanometer Sized Metals on Cadmium Sulfide Surfaces*. Ed. by Ridderprint BV. Vol. 1. 2019. Chap. 2, pp. 11–17. 7 pp. ISBN: 9789463752343.

[29] Holthausen M.C. Koch W. *A Chemist's Guide to Density Functional Theory*. 2nd ed. Varrentrappstraße 40-42 D-60485 Frankfurt Germany, Hans-Meerwein-Straße D-35032 Marburg Germany: Wiley-VCH, 2008. Chap. 5, pp. 41–47. ISBN: 9783527303724.

[30] Hafner J. Kresse G. "Ab initio molecular dynamics for liquid metals". In: *Physical Review B* 47.1 (Jan. 1993), p. 558. DOI: https://doi.org/10.1103/PhysRevB.47.558.

[31] Hafner J. Kresse G. "Ab initio molecular-dynamics simulation of the liquid-metal–amorphous-semiconductor transition in germanium". In: *Physical Review B* 49.20 (May 1994), p. 14251. DOI: https://doi.org/10.1103/PhysRevB.49.14251.

[32] Furthmüller J. Kresse G. "Efficiency of ab-initio total energy calculations for metals and semiconductors using a plane-wave basis set". In: *Computational materials science* 6.1 (June 1996), pp. 15–50. DOI: https://doi.org/10.1016/0927-0256(96)00008-0.

[33] Georg Kresse and Jürgen Furthmüller. "Efficient iterative schemes for ab initio total-energy calculations using a plane-wave basis set". In: *Physical review B* 54.16 (Oct. 1996), p. 11169. DOI: https://doi.org/10.1103/PhysRevB.54.11169.

[34] Ernzerhof M. Perdew J.P. Burke K. "Generalized gradient approximation made simple". In: *Physical review letters* 77.18 (1996), p. 3865. DOI: https://doi.org/10.1103/PhysRevLett.77.3865. URL: https://journals.aps.org/prl/abstract/10.1103/PhysRevLett.77.3865.

[35] Ernzerhof M. Perdew J.P. Burke K. "Erratum: Generalized gradient approximation made simple". In: *Physical review letters* 78 (1997), p. 1396.

[36] *VASP the GUIDE*. URL: https://cms.mpi.univie.ac.at/vasp/vasp/vasp.html.

[37] Koster R.S. Klimes J.-van Blaaderen A.-van Huis M. Fang C. Li W. "The accurate calculation of the band gap of liquid water by means of GW corrections applied to plane-wave desnity functional theory molecular dynamics simulations". In: *The Journal of Chemical Physics* 17.365 (2015). DOI: 10.1039/c4cp04202f.

[38] Tkatchenko A. Alfe D.-Slater B. Michealides A. Car R. Scheffler M. Santra B. Klimes J. "On the accuracy of van der Waals inculsive density-funcional theory exchange-correlation functionals for ice at ambient and high pressures". In: *The Journal of Chemical Physics* 139.154702 (2013). DOI: 10.1063/1.4824481. eprint: http://dx/doi.org/10.1063/1.4824481. URL: https://www.researchgate.net/publication/265250897_JChemPhys_139_154702_2013.

[39] Michaelides A. Klimes J. Bowler D.R. "Van der Waals density functionals appiled to solids". In: *Physics review Lettre.* 83 (2011). DOI: 195131. URL: https://journals.aps.org/prb/abstract/10.1103/PhysRevB.83.195131.

[40] Li S. Puzder A.-Hyldgaard P. Langreth D. C. Thonhauser T. Cooper V.R. "Van der Waals density functional: Self-consistent potential and the nature of the van der Waals bond". In: *Physics review Lettre.* 76 (2007). DOI: 10.1103. URL: https://journals.aps.org/prb/abstract/10.1103/PhysRevB.76.125112.

[41] Ehrlich S. Krieg H. Grimme S. Antony J. "A consistent and accurate ab initio parametrization of density functional dispersion correction (DFT-D) for the 94 elements H-Pu". In: *The Journal of Chemical Physics* 132.15 (2010). DOI: 10.1063. eprint: https://doi.org/10.1063/1.3382344. URL: https://aip.scitation.org/doi/pdf/10.1063/1.3382344.

[42] SchrÖder E. Langreth D. C. Lundqvist B. I. Dion M. Rydberg H. "Van der Waals Density Functional for General Geometries". In: *American Physical Society* 92.24 (2004). DOI: 10.1103. eprint: https://doi.org/10.1103/PhysRevLett.92.246401. URL: https://journals.aps.org/prl/abstract/10.1103/PhysRevLett.92.246401.

[43] Michaelides A. Klimes J. Bowler D.R. "Chemical accuracy for the van der Waals density functional". In: *Journal of Physical Condensed Matter* 2.22 (2009). DOI: 10.1088/0953-8984/22/2/022201. URL: https://www.ncbi.nlm.nih.gov/pubmed/21386245.

[44] Österbacka R. Majumdar S. Majumdar H.S. *Comprehensive Nanoscience and Technology.* Vol. 1. 2011. Chap. 1.05.2.2.1, pp. 109–142. DOI: 10.1016.

[45] Li M. A step-by-step tutorial of SOC calculations with VASP. In: Oct. 2017.

[46] Torres W.S. Timmermans M. Costache M.V. Valenzuela S.O. Benítez L.A. Sierra J.F. "Investigating the spin-orbit interaction in van der Waals heterostructures by means of the spin relaxation anisotropy". In: *Journal of Applied Physics* 7 (12 Dec. 2019). DOI: https://doi.org/10.1063/1.5124894.

[47] M. A. Li W. Fang C. van Huis. "Strong spin-orbit splitting and magnetism of point defect states in monolayer WS_2". In: *Phys. Rev. B* 94 (19 2016). DOI: 10.1103/PhysRevB.94.195425. URL: https://link.aps.org/doi/10.1103/PhysRevB.94.195425.

[48] Fan H. Liu X. "Electronic structure, elasticity, Debye temperature and anisotropy of cubic WO3 from first-principles calculation". In: *Royal Society open science* 5.6 (June 2018), p. 171921. DOI: https://doi.org/10.1098/rsos.171921.

[49] Shiau L.L. Krivosheeva A. Shaposhnikov V. Borisenko V. Gusakov V. Tay B.K. Gusakova J. Wang X. "Electronic Properties of Bulk and Monolayer TMDs: Theoretical Study Within DFT Framework (GVJ-2e Method". In: *applications and materials science* 214 (12 Sept. 2017). DOI: https://doi.org/10.1002/pssa.201700218. URL: https://onlinelibrary.wiley.com/doi/abs/10.1002/pssa.201700218.

[50] Graivoronskaya E.A. Solonin Y. M. Khyzhun O. Y. "Nonstoichiometric tungsten oxide based on hexagonal WO3". In: *Crystal Growth & Design* 1.6 (Oct. 2001), pp. 473–477. DOI: https://doi.org/10.1021/cg015545z.

A Benchmarking Results

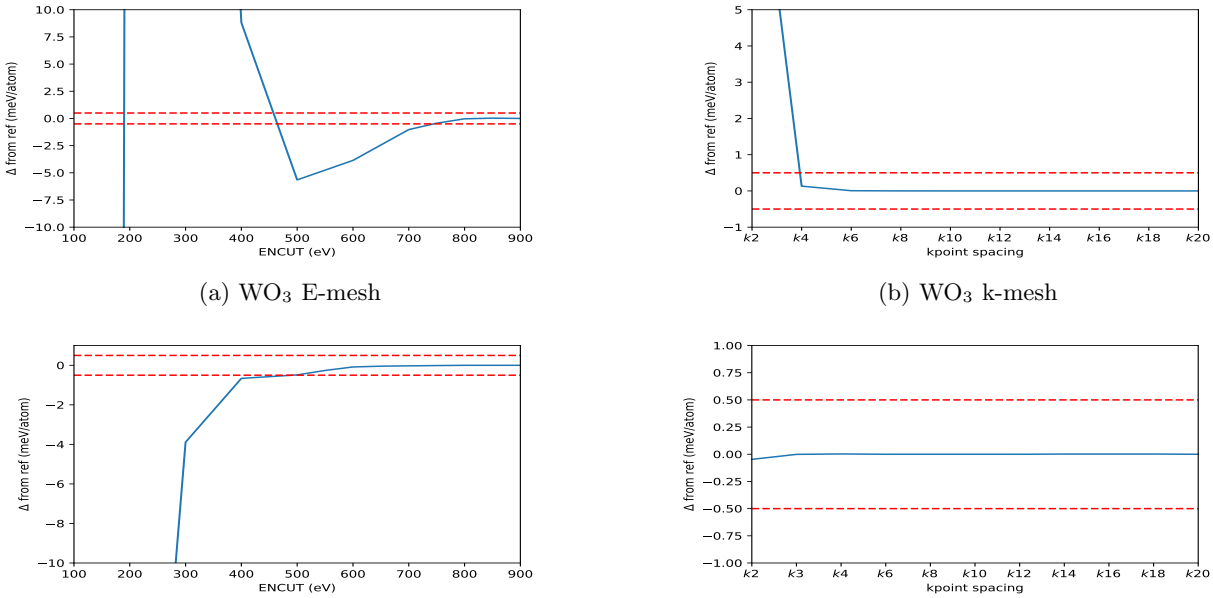

(a) WO_3 E-mesh

(b) WO_3 k-mesh

(c) WS_2 E-mesh

(d) WS_2 k-mesh

Figure 7: These are the ENCUT and k-point meshes of WO_3 and WS_2. On the vertical axis the energy difference from the reference is represented (meV/atom). While on the x-axis, we represent what ENCUT value or which k-point spacing we are looking at. Here the smallest index in k-space is used to represent the k-point spacing. The blue lines represent the energy of the samples and the red lines indicate the accuracy range we wish to achieve.

Based on the results in figure 7, the best values for ENCUT and the k-spacing have been determined. These values need to be within ±0.5 meV/atom of the reference value in order to be accurate enough. To maintain high accuracy, the second value that is within this interval is taken instead of the first, since there is both an uncertainty in the k-point spacing and in the energy mesh. Two optimisations need to be done, if the first value within the ±0.5 meV/atom is taken in both scenarios it is more likely that the uncertainty will deviate more than 0.5 meV/atom from the reference value. This gives for WO_3 an ENCUT value of 800 and a k-point spacing of 12x12x6. This gives for WS_2 an ENCUT value of 550 and a k-point spacing of 12x12x4. These values will be used for further DFT calculations.

B Additional images

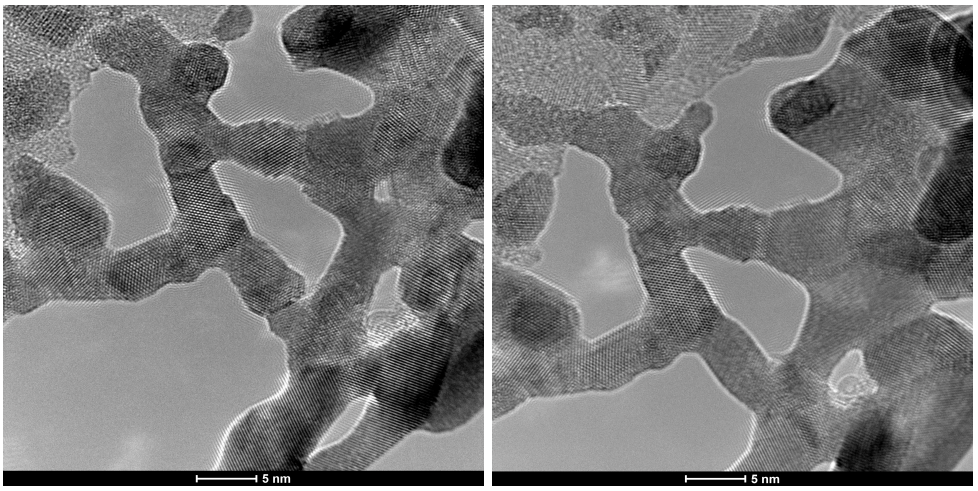

(a) before lattice matching (b) after lattice matching

Figure 8: Lattice matching of different areas at 800 °C. In the middle of the image where 3 section comes together there is a lattice mismatch in fig (a), while there is a lattice match in fig (b) for the same area.

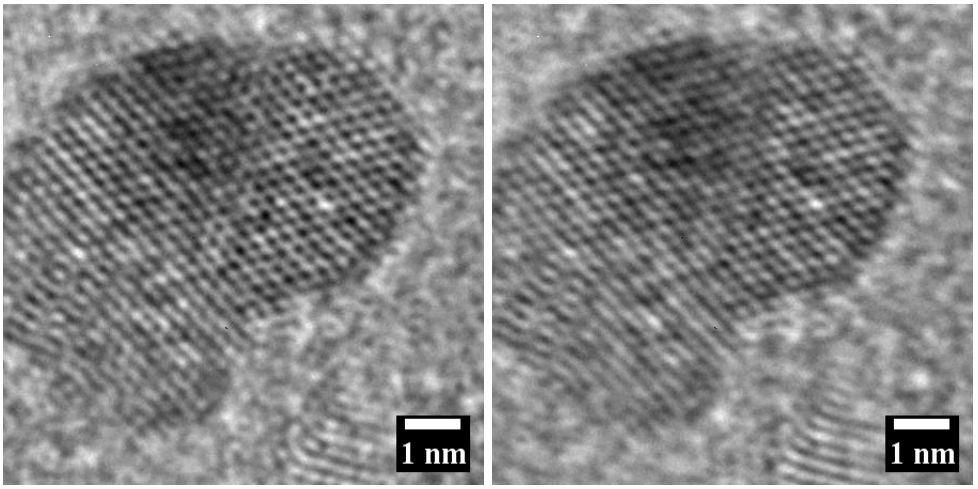

(a) intial state (b) final state

Figure 9: The structure becomes faceted at 800 °C. Images are obtained from one video. In fig (a) the lattice lacks structure, in fig (b) the lattice is faceted. The final state has better defined angles in its structure.

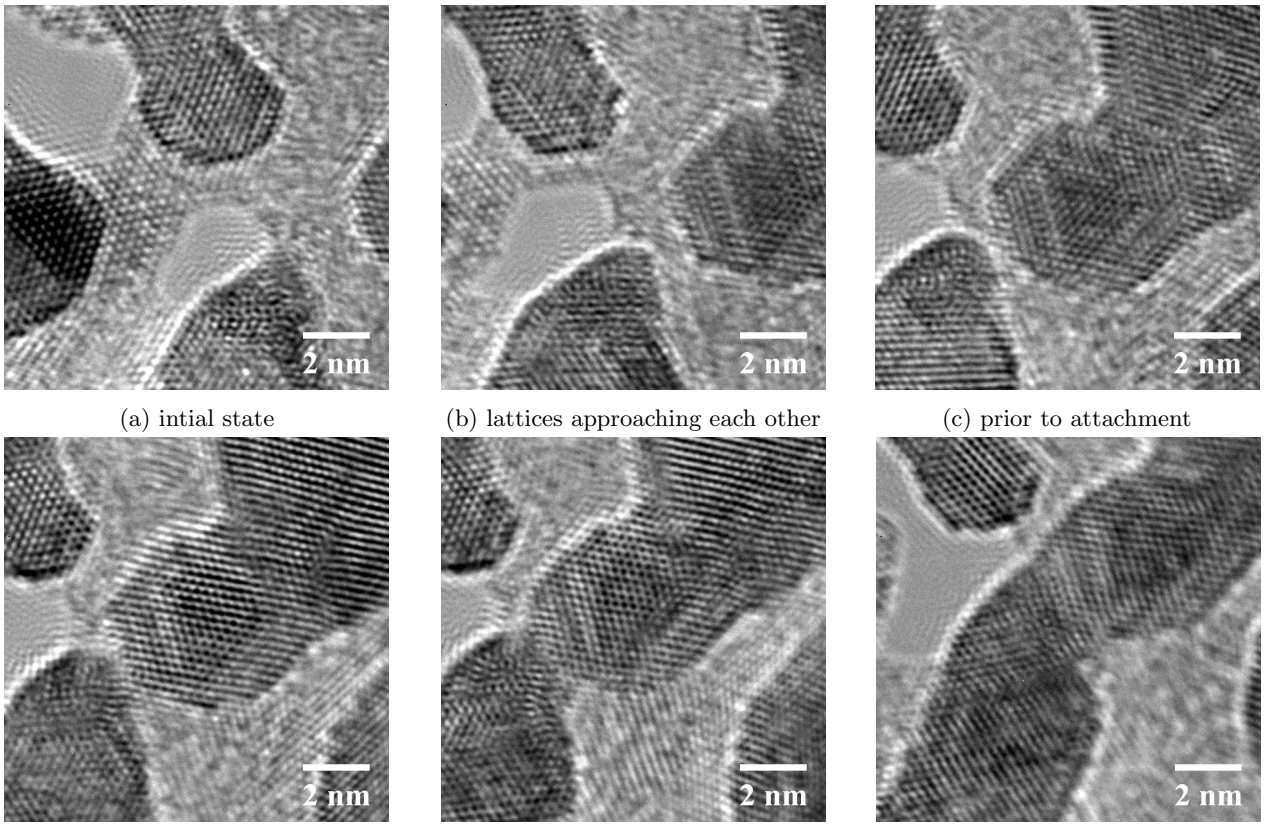

(a) intial state (b) lattices approaching each other (c) prior to attachment

(d) first step of attachment (e) lattices are attached, but there is still a lattice mismatch (f) lattices are matched, oriented attachement has occured

Figure 10: Oriented attachment occuring at 800 °C. The images were obtained from one video.

C Spin-Orbit Coupling

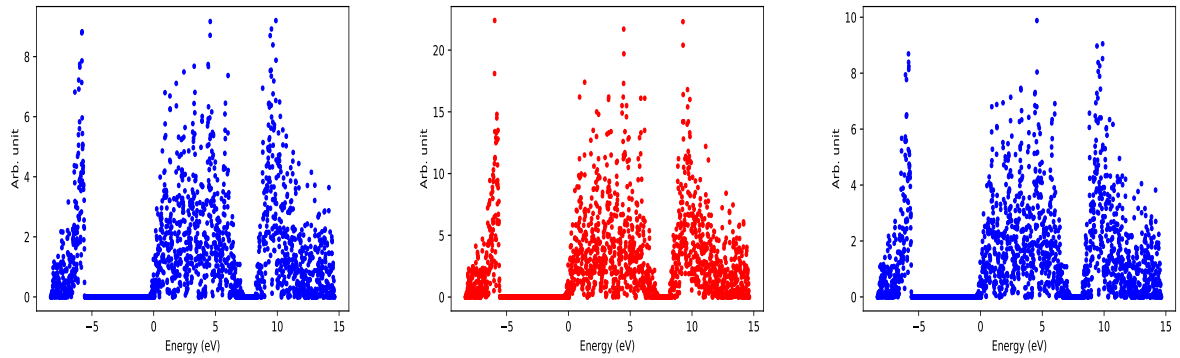

(a) AFM with 2 μ_B as initial magnetic moment, without SOC

(b) AFM with 2 μ_B as initial magnetic moment, with SOC

(c) AFM with 4 μ_B as initial magnetic moment, without SOC

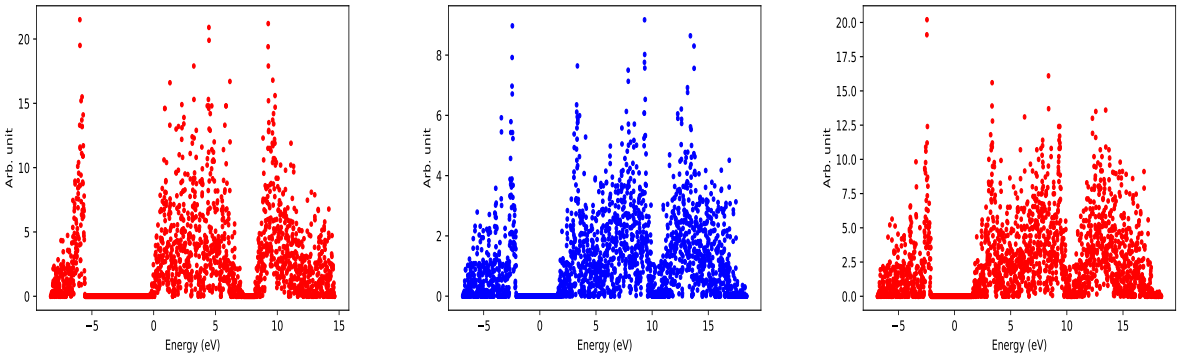

(d) AFM with 4 μ_B as initial magnetic moment, with SOC

(e) FM with 4 μ_B as initial magnetic moment, without SOC

(f) FM with 4 μ_B as initial magnetic moment, with SOC

Figure 11: The difference SOC makes on the Density of State of WS_2 for different initial magnetic moments. The blue and red graphs are with and without SOC respectively

D Band structures

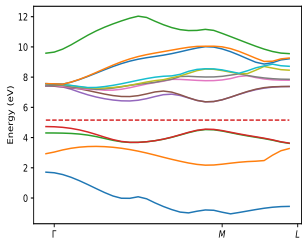

(a) non-magnetic WS_2

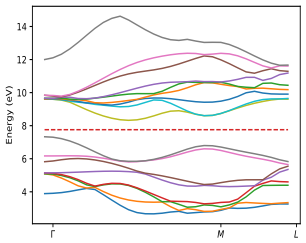

(b) AFM WS_2 with 2 μ_B as initial magnetic moment

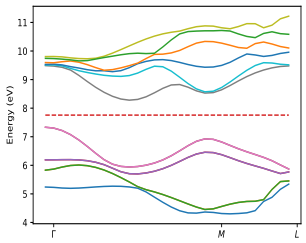

(c) AFM WS_2 with 2 μ_B as initial magnetic moment, including SOC

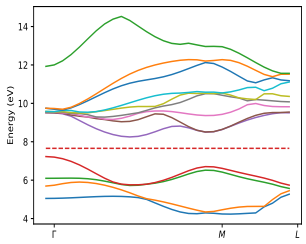

(d) AFM WS_2 with 4 μ_B as initial magnetic moment

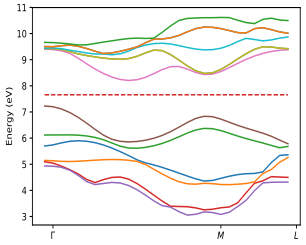

(e) AFM WS_2 with 4 μ_B as initial magnetic moment, including SOC

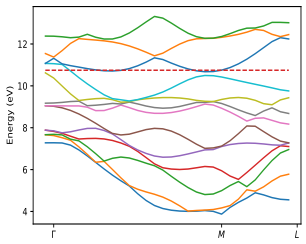

(f) FM WS_2 with 4 μ_B as initial magnetic moment

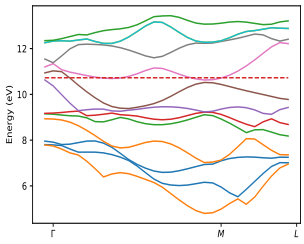

(g) FM WS_2 with 4 μ_B as initial magnetic moment, including SOC

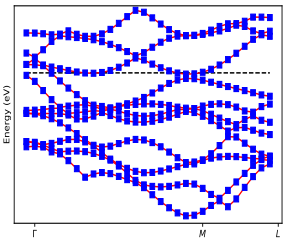

(h) FM WS_2 with 4 μ_B as initial magnetic moment, with spin

Figure 12: Band structures for different magnetic moments of WS_2, the red dashed line represents the fermi-energy. Blue squares are used to represent the spin up states and a red line to represent the spin down states.